

UNIVERSITÀ DEGLI STUDI DI UDINE

Università degli studi di Udine

Transfer-Matrix modeling of the Access Region Resistance in Graphene based Dirac-Source FETs

Original

Availability:
This version is available http://hdl.handle.net/11390/1299064 since 2025-01-24T07:41:24Z

Publisher:

Published
DOI:10.1109/JEDS.2025.3533599

Terms of use:
The institutional repository of the University of Udine (http://air.uniud.it) is provided by ARIC services. The aim is to enable open access to all the world.

Publisher copyright

(Article begins on next page)

22 November 2026

Transfer-Matrix modeling of the Access Region Resistance in Graphene based Dirac-Source FETs

Erica Baccichetti and David Esseni, *Fellow, IEEE*
DPIA, University of Udine, Udine, Italy.

***Abstract*—In this paper we first present a model based on the transfer-matrix methodology to describe the ballistic resistance in a graphene p–n junction, and employ the model in Dirac-Source FETs. In fact, the access region of a graphene based Dirac-Source FET includes a p–n junction, and we show that this has a sizeable impact on the on-state current of these transistors. In particular, we first validate our model by comparing the calculated p–n junction resistance with previous experiments and simulations. Then, we exploit the transfer-matrix description into a virtual-source model for nanoscale Dirac-Source FETs, and discuss the influence on the I_{DS}-V_{GS} curves of the p–n junction that is embedded in the access region of the device.**

***Index Terms*—Graphene, Dirac materials, Transport modelling, Transfer-Matrix, Dirac-Source FETs.**

I. Introduction

As the CMOS technology is approaching the 1 nm node, the energy efficiency has become paramount [1]. Innovations at material and device level are required to devise CMOS transistors capable of switching at a greatly reduced energy. To this purpose, a V_{DD} scaling to about 0.3 V would be extremely beneficial [2], but this is hindered by the thermionic emission of carriers from source, which dictates a sub-threshold swing of CMOS FETs no smaller than 60 mV/dec at room temperature [3].

Dirac semi-metals, like graphene, have a Density of States (DoS) proportional to $|E-E_D|$ close to the Dirac energy E_D [4] (see Fig. 1(a)). Hence, in the p–type source of an n–type graphene Dirac-Source FET (DS-FET), the electron density $n(E)$ decays more steeply than the Boltzmann tail of the Fermi-Dirac function for energies $E>E_{F,S}$. Fig. 1 illustrates a comparison between the energy relation, the density of states DoS(E), and the energy spectrum $n(E)$ of electrons, in a graphene source and in a source consisting of a conventional 3D semiconductor.

Differently from Tunnel FETs, the sub-thermionic transport mechanism in DS-FETs does not rely on tunnelling, hence a large drive current has been singled out as a distinct advantage of this intriguing device concept [1].

©2025 IEEE. Personal use of this material is permitted. Permission from IEEE must be obtained for all other uses, in any current or future media, including reprinting/republishing this material for advertising or promotional purposes, creating new collective works, for resale or redistribution to servers or lists, or reuse of any copyrighted component of this work in other works.
DOI: 10.1109/JEDS.2025.3533599

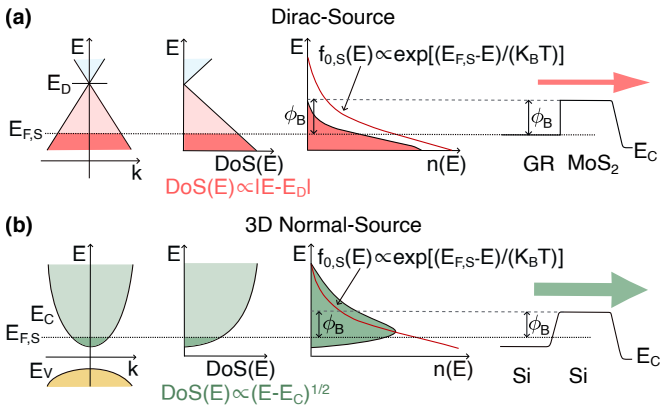


Figure 1: **(a)** Graphene. Schematic band structure close to the Dirac energy E_D, corresponding DoS(E), electron density $n(E)$, and thermionic electron emission over a potential energy barrier. For $E>E_{F,S}$, the energy spectrum $n(E)$ of the electron density in graphene decays more steeply than the Fermi-Dirac occupation function $f_{0,S}(E)$. **(b)** Same as in (a), but for a conventional 3D semiconductor described by the effective mass approximation. The DoS and $n(E)$ are shown close to the minimum E_C of the conduction band, where the Dos(E) is proportional to $(E-E_C)^{1/2}$ and the electron energy spectrum $n(E)$ decays roughly as $f_{0,S}(E)$.

Experimental reports established the feasibility of graphene DS-FETs [5, 6, 7], and numerical simulations were used to investigate the device operation and performance [8]. Moreover, design guidelines for DS-FETs were recently proposed in [9], where the calculated I_{DS} values approach 1mA/μm at V_{DS}=0.3 V and ($V_{GS}-V_T$)≈0.6 V. Such predictions, however, neglect the finite ballistic conductance of the graphene p–n junction in the access region [9].

We here extend our previous work on the access region resistance in DS-FETs [10], and we present in more details the semi-analytical model for the graphene p–n junction resistance, based on a rigorous transfer-matrix methodology. A transfer matrix model for graphene was previously used for transport in graphene nanoribbon superlattices [11]. Our calculations for the p–n junction resistance are first validated against experiments, and then used to discuss the impact on the I_{DS}-V_{GS} curves of DS-FETs of the resistance in the access region of the device. Our results suggest that the source access region plays a critical role to attain competitive I_{ON} values in

nanoscale DS-FETs.

II. Transfer Matrix Model in Graphene

The electronic properties of graphene for energies fairly close to the Dirac energy E_D can be described by the time-dependent, Dirac-like equation:

$$i\hbar\frac{\partial}{\partial t}\begin{pmatrix}\varphi_1(\bar{r},t)\\ \varphi_2(\bar{r},t)\end{pmatrix}=\hat{H}_{2D}\begin{pmatrix}\varphi_1(\bar{r},t)\\ \varphi_2(\bar{r},t)\end{pmatrix} \tag{1}$$

where $\bar{r}$=(x,y) is the position in the graphene plane, and the Hamiltonian operator is given by [12, 4]:

$$\hat{H}_{2D}=-i\hbar v_f\left(\sigma_x\frac{\partial}{\partial x}+\sigma_y\frac{\partial}{\partial y}\right)+I_2\,U_D(\bar{r}). \tag{2}$$

In Eq. (2), $v_f\simeq 8.8\cdot 10^7$cm/s denotes the Fermi velocity, σ_x and σ_y are the Pauli matrices and I_2 is the two-by-two identity matrix. The wave-function is thus a two-component spinor $\overline{\varphi}(\bar{r},t)=\begin{pmatrix}\varphi_1(\bar{r},t)\\ \varphi_2(\bar{r},t)\end{pmatrix}$, and the probability flux $\bar{J}_{\bar{\varphi}}(\bar{r},t)$ can be derived from Eq. (1) leading to (see Appendix A):

$$(J_{\bar{\varphi},x},J_{\bar{\varphi},y})=v_f\left[\varphi_1^*\varphi_2+\varphi_1\varphi_2^*,-i\left(\varphi_1^*\varphi_2-\varphi_1\varphi_2^*\right)\right]. \tag{3}$$

The $\bar{r}$ and t dependence of the wave-function can be separated as $\overline{\varphi}(\bar{r},t)=\overline{\psi}(\bar{r})exp\left(-i\left(Et/\hbar\right)\right)$, where $\overline{\psi}(\bar{r})$ fulfills the time-independent Dirac equation $\hat{H}_{2D}\overline{\psi}(\bar{r})=E\overline{\psi}(\bar{r})$.

For a potential energy $U_D(x)$ that varies only along x, the momentum along y is conserved and we can make the usual *ansatz* $\overline{\psi}(\bar{r})=\begin{pmatrix}\psi_1(x)\\ \psi_2(x)\end{pmatrix}e^{ik_y y}$, which brings us to the Dirac-like equations

$$-i\hbar v_f\left(\frac{\partial}{\partial x}\psi_2+k_y\psi_2\right)+U_D(x)\,\psi_1=E\,\psi_1 \tag{4a}$$

$$-i\hbar v_f\left(\frac{\partial}{\partial x}\psi_1-k_y\psi_1\right)+U_D(x)\,\psi_2=E\,\psi_2 \tag{4b}$$

For any energy E and transverse momentum $\hbar k_y$, Eq. (4) provides $\psi_1(x)$, $\psi_2(x)$ and thus the overall wave-function.

For a region where $U_D(x)$=U_0 is constant, Eq. (4) can be solved analytically, as it is described in more details in Appendix B. More explicitly, for $E>[U_0+\hbar v_f|k_y|]$ or $E<[U_0-\hbar v_f|k_y|]$, we define

$$k_x=\sqrt{\left(\frac{E-U_0}{\hbar v_f}\right)^2-k_y^2} \tag{5}$$

and Eq. (4) has the propagating solutions [12, 4]

$$\psi_1(x)=A\,e^{ik_x x}+B\,e^{-ik_x x} \tag{6a}$$

$$\psi_2(x)=s_{cv}\,A\,e^{i(k_x x+\theta_{\bar{k}})}-s_{cv}\,B\,e^{-i(k_x x+\theta_{\bar{k}})} \tag{6b}$$

where s_{cv} is 1.0 if $E>U_0$, while it is -1.0 if $E<U_0$, namely s_{cv}=sign($E-U_0$). Moreover, the angle $\theta_{\bar{k}}$ is defined as $\theta_{\bar{k}}$=arctan(k_y/k_x), whereby Eq. (5) ensures that k_x is non negative.

For $U_0-\hbar v_f|k_y|<E<U_0+\hbar v_f|k_y|$, instead, we define

$$\gamma_x=\sqrt{k_y^2-\left(\frac{E-U_0}{\hbar v_f}\right)^2},\ \xi=\text{sign}(k_y)\sqrt{\left|\frac{k_y-\gamma_x}{k_y+\gamma_x}\right|} \tag{7}$$

and Eq. (4) has the evanescent solutions

$$\psi_1(x)=Ae^{\gamma_x x}+Be^{-\gamma_x x} \tag{8a}$$

$$\psi_2(x)=i\,s_{cv}\,\xi\,A\,e^{\gamma_x x}+i\,s_{cv}\,\xi^{-1}\,B\,e^{-\gamma_x x} \tag{8b}$$

As it can be seen, the conservation of $\hbar k_y$ opens an effective energy gap which is $2\hbar v_f|k_y|$ wide, as it is depicted in Fig. 2a.

The propagating solutions in Eq. (6) can be used to calculate analytically the transmission $T(E,k_y)$ across a rectangular potential energy barrier. This leads to the Klein tunnelling condition whereby, for k_y=0, the transmission $T(E,k_y)$ tends to 1.0 irrespective of the energy barrier height [12].

Moreover, Eq. (6) and Eq. (8) can be used to calculate $T(E,k_y)$ for an arbitrary $U_D(x)$ profile by using a transfer matrix approach. If we consider, for example, the $U_D(x)$ in Fig. 2a corresponding to a graphene *p–n* junction, we can discretize $U_D(x)$ with the L_J elements defined by $x_J<x<x_{J+1}$ (with J=$0,1\cdots N-1$) and use Eq. (6) or Eq. (8) in each L_J element. Then, by imposing the continuity of $\psi_1(x_J)$ and $\psi_2(x_J)$ at each x_J, we obtain a linear relation between the A, B coefficients in the L_{J-1} and in the L_J element:

$$\begin{pmatrix}A_{J-1}\\ B_{J-1}\end{pmatrix}=[M_{J-1,J}]\begin{pmatrix}A_J\\ B_J\end{pmatrix}. \tag{9}$$

Here we note that, for the Dirac-like graphene Hamiltonian, the probability flux has the expression in Eq. (3), which does not involve the derivative of ψ_1, ψ_2. Therefore, the continuity of ψ_1, ψ_2 ensures the continuity of the probability flux.

Based on Eq. (9), we can readily link the A, B coefficients in the first and last section as $\begin{pmatrix}A_0\\ B_0\end{pmatrix}=[MT]\begin{pmatrix}A_N\\ B_N\end{pmatrix}$, where the 2×2 transmission matrix $[MT]$ is defined as

$$[MT(E,k_y)]=\begin{bmatrix}MT_{1,1} & MT_{1,2}\\ MT_{2,1} & MT_{2,2}\end{bmatrix}=\prod_{J=1}^{N}M_{J-1,J}. \tag{10}$$

The elements of $[MT]$ depend on E and k_y, and they can be used to calculate the transmission $T(E,k_y)$, defined as the ratio between the probability fluxes along the positive x direction in section N and in section 0. By doing so (see Appendix B), the $T(E,k_y)$ can be expressed as:

$$T(E,k_y)=\frac{k_{x,N}}{k_N}\frac{k_0}{k_{x,0}}\,|t|^2 \tag{11}$$

where k_0, k_N are the magnitude and $k_{x,0}$, $k_{x,N}$ are the x component of the wave-vector respectively in section 0 and N (see Fig. 2a). The wave-vectors k_0, $k_{x,0}$, k_N, $k_{x,N}$ are uniquely set by E, k_y and by the Dirac energies $U_D(x_0)$, $U_D(x_N)$ in section 0 and N.

As for the term $|t|^2$ in Eq. (11), we argue that $|t|^2$ can be identified as one of the elements of the matrix $[MT]$ in Eq. (10), which is unambiguously determined by E, k_y, $U_D(x_0)$, $U_D(x_N)$. For example, if $E<[U_D(x_0)-\hbar v_f|k_y|]$ and $E>[U_D(x_N)+\hbar v_f|k_y|]$ (as depicted in Fig. 2a), then the energy E belongs to the valence band in section 0 and to the conduction band in section N. In this case, in section 0 the probability flux in the positive x direction is carried by $B_0\,e^{-ik_x x}$ and the flux in the in the negative x direction is carried by $A_0\,e^{ik_x x}$ (see Appendix B). In section N, instead,

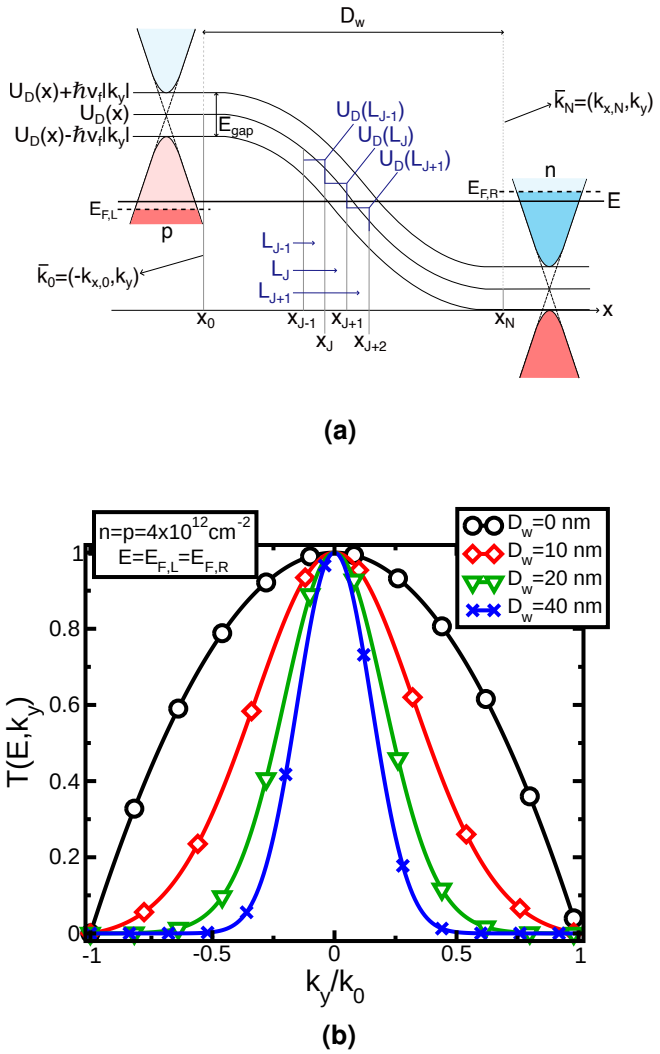


Figure 2: **(a)** Band diagram for a p–n graphene junction, showing also the energy levels $[U_D(x)+\hbar v_f|k_y|]$ and $[U_D(x)-\hbar v_f|k_y|]$ that identify a $2\,\hbar v_f|k_y|$ wide effective energy gap (see main text). Staircase approximation for $U_D(x)$ used for the transfer matrix method described in Section II. **(b)** Corresponding transmission calculated from Eq. (11) versus k_y/k_0 (with $k_0{=}|\bar{k}_0|{=}|E{-}U_D(x_0)|/(\hbar v_f)$) and for the energy $E{=}E_{F,L}{=}E_{F,R}$. Results for $n{=}p{=}4{\cdot}10^{12}\text{cm}^{-2}$ and for different transition widths D_W.

the flux in the positive x direction is carried by $A_N\,e^{ik_x x}$ and the flux in the negative x direction is carried by $B_N\,e^{-ik_x x}$. Therefore, in order to determine $T(E,k_y)$ one can set $B_N{=}0$, corresponding to zero probability flux in the negative x direction in section N, and obtain $|t|^2{=}|A_N|^2/|B_0|^2{=}1/|MT_{2,1}|^2$. The other three possible cases are similar and identify a different element of the matrix $[MT]$, as it is summarized in Table I.

Fig. 2b displays the $T(E,k_y)$ of a $p{-}n$ junction calculated from Eq. (11) and reported versus k_y/k_0, where $k_0{=}|E{-}U_D(x_0)|/(\hbar v_f)$ is the magnitude of the wave-vector in the first section. For $k_y{=}0$ the $T(E,k_y)$ is 1.0 irrespective of D_W, which is analogous to the Klein tunnelling condition

Section 0	Section N	$\lvert t\rvert^2$
$E{>}U_D(x_0){+}\hbar v_f\lvert k_y\rvert$	$E{>}U_D(x_N){+}\hbar v_f\lvert k_y\rvert$	$\frac{\lvert A_N\rvert^2}{\lvert A_0\rvert^2}{=}\frac{1}{\lvert MT_{1,1}\rvert^2}$
$E{>}U_D(x_0){+}\hbar v_f\lvert k_y\rvert$	$E{<}U_D(x_N){-}\hbar v_f\lvert k_y\rvert$	$\frac{\lvert B_N\rvert^2}{\lvert A_0\rvert^2}{=}\frac{1}{\lvert MT_{1,2}\rvert^2}$
$E{<}U_D(x_0){-}\hbar v_f\lvert k_y\rvert$	$E{>}U_D(x_N){+}\hbar v_f\lvert k_y\rvert$	$\frac{\lvert A_N\rvert^2}{\lvert B_0\rvert^2}{=}\frac{1}{\lvert MT_{2,1}\rvert^2}$
$E{<}U_D(x_0){-}\hbar v_f\lvert k_y\rvert$	$E{<}U_D(x_N){-}\hbar v_f\lvert k_y\rvert$	$\frac{\lvert B_N\rvert^2}{\lvert B_0\rvert^2}{=}\frac{1}{\lvert MT_{2,2}\rvert^2}$

Table I: Energy dependent choice of the element of the $[MT]$ matrix to be used in the calculation of the transmission coefficient $T(E,k_y)$. As explained in Appendix B, for $E{>}(U_D(x_N){+}\hbar v_f|k_y|)$ we assume $B_N{=}0$ and for $E{<}(U_D(x_N){-}\hbar v_f|k_y|)$ we assume instead $A_N{=}0$.

[12].

Once the $T(E,k_y)$ is known, the current for a two terminal device can be obtained from the well-known Landauer model [13], that for a 2D electron gas provides

$$I_{LR}=\frac{2n_v q}{h}\frac{W_y}{2\pi}\int_{-\infty}^{+\infty}dE\int_{-\infty}^{+\infty}dk_y\,T(E,k_y)[f_{0,R}-f_{0,L}] \quad (12)$$

where n_v is the valley degeneracy ($n_v{=}2$ in graphene), q is the electron charge, W_y is the device width. The symbols $f_{0,L}(E)$, $f_{0,R}(E)$ denote the Fermi functions of respectively the left and right reservoir, with $E_{F,R}{=}(E_{F,L}{-}q\text{V}_{RL})$ (see Fig. 2a). The integral over k_y in Eq. (12) can be restricted to $|k_y|{\le}\min(k_0,k_N)$ with $k_{0(N)}{=}|E{-}U_D(x_{0(N)})|/(\hbar v_f)$, because $\min(k_0,k_N)$ is the maximum $|k_y|$ corresponding to propagating solutions in both the left and the right hand graphene region.

Eq. (12) has a wide validity but it neglects inelastic scattering [13]. In fact, the DS-FET itself relies on the fact that electrons injected from the Dirac source can travel ballistically to the energy barrier shown in Fig. 1(a) [5, 8, 6, 9]. This scenario is favoured by the very large room temperature mean free path of graphene, which is about 150-200 nm for graphene on common substrates (SiO2, SiC) [14], and up to 500 nm for CVD graphene between hBN layers [15].

III. Resistance in a graphene p–n junction

Assuming a very small voltage V_{LR}, we can expand $(f_{0,R}{-}f_{0,L})$ in Eq. (12) to first order in V_{LR} and then calculate the linear resistance of the p–n junction $R_{LR}{=}V_{LR}/I_{LR}$. This readily leads to

$$R_{LR}=\frac{hK_BT}{2n_vq^2}\frac{2\pi}{W_y}\cdot \cdot\frac{1}{\int_{-\infty}^{+\infty}dE\int_{-\infty}^{+\infty}dk_yT(E,k_y)f_{0,R}[1-f_{0,R}]} \quad (13)$$

A. Comparison with previous calculations

In Fig. 3 we show the linear resistance as a function of $(U_{D,L}{-}U_{D,R})$, where $U_{D,L}$ and $U_{D,R}$ are respectively the Dirac energy in the left and right regions of a graphene junction, as the one sketched in Fig. 2a. The results are

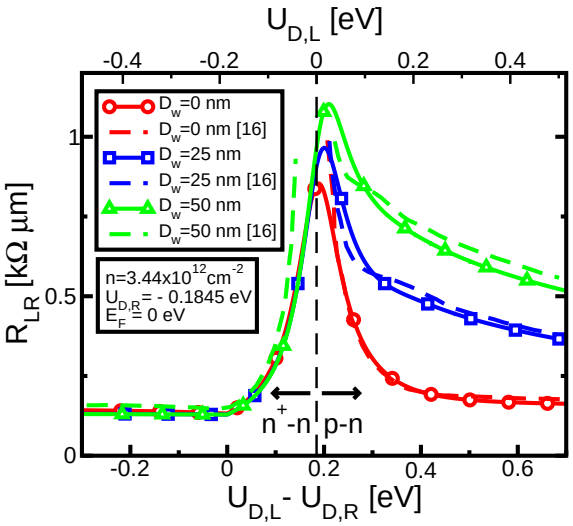


Figure 3: Linear resistance of a graphene junction versus $(U_{D,L}-U_{D,R})$ for different D_W values. The carrier density in the n-type region is set to n=3.44 · 10^{12} cm^{-2} which, for $E_{F,L}$=$E_{F,R}$=E_F=0 eV, corresponds to $U_{D,R}\simeq-0.1845$ eV.

reported for different values of the width D_W of the transition from the left to the right region and assuming a linear profile of the Dirac energy (namely the electrostatic potential) in the transition region. The carrier density in the right region is fixed at $n\simeq3.44\cdot10^{12}$ cm^{-2}, corresponding to $U_{D,R}\simeq-0.1845$ eV in the near-equilibrium conditions where $E_{F,R}\simeq E_{F,L}$=0 eV.

Fig. 3 compares the results of our simulations to those reported in [16]. The maximum resistance is observed for $(U_{D,L}-U_{D,R})\approx0.1845$ eV, corresponding to $U_{D,L}\approx E_{F,L}$=0 and thus to a very low carrier density and high resistance in the left region. The resistance calculations in [16] employed the zero temperature limit, so that the resistance has a singularity for $U_{D,L}\approx$0, which is not observed in our results because Eq. (13) accounts for a finite temperature, and we used T=300 K in all our calculations, unless otherwise stated.

Except for the condition $(U_{D,L}-U_{D,R})\approx0.1845$ eV, our results are in good agreement with [16] [1], which validates the model developed in this work. In particular, for $(U_{D,L}-U_{D,R})<0.1845$ eV, we have an n^+-n rather than a p-n junction, hence the resistance is smaller than it is for $(U_{D,L}-U_{D,R})>0.1845$ eV. An actual p-n junction exists instead for $(U_{D,L}-U_{D,R})>0.1845$ eV, in which case the resistance becomes sensitive to the width of the p-n transition and it appreciably increases for larger D_W values.

B. Comparison with experimental data

The resistance of graphene p–n junctions has been experimentally studied in [17], by using the test-structure sketched in Fig. 4a. The voltage V_B at the back gate sets the electron density n_1 in the regions 1. The top gate voltage V_T, instead, sets the carrier density c_2 in region 2, which can be either

[1]In [16] the values of resistance are refered to the series of two junctions so we multiplied our results by two in order to make a comparison.

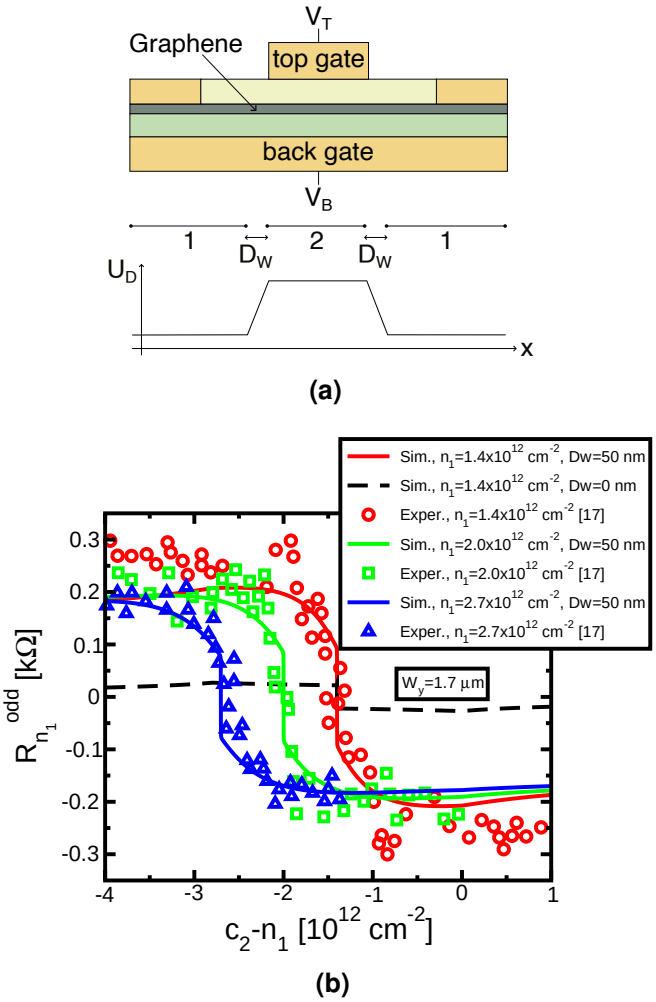


Figure 4: **(a)** Sketch of the structure employed in [17] to investigate the resistance in graphene p–n junctions. **(b)** Odd resistance versus (c_2-n_1) for different n_1 values; c_2 is defined in the text. The device width is W_y=1.7 μm and the temperature is T=4 K. Symbols are experiments from [17], and solid lines are our simulations for a p–n junction width D_W=50 nm. The dashed black line shows the calculated R_{n1}^{odd} for an abrupt p–n junction with D_W=0.

p– or n–type. By following [17], we here define c_2=$-p_2$<0 if region 2 is p–type, and c_2=n_2>0 if region 2 is n–type. For a given V_B and n_1, the measured resistance $R_{n1}(c_2)$ is larger when region 2 is p–type [17]. In other words, $R_{n1}(c_2)$ is larger when there exists p–n junctions along the current path in Fig. 4a. To isolate the p–n junction resistance in the measured overall resistance of the test structure in Fig. 4a, the *odd resistance* R_{n1}^{odd} was defined as [17]

$$R_{n1}^{odd}(c_2)=[R_{n1}(c_2)-R_{n1}(-c_2)]/2 \qquad (14)$$

and employed in the analysis of the experiments.

We calculated R_{n1}^{odd} by using the resistance $R_{n1}(c_2)$ calculated from Eq. (13). Fig. 4b compares our simulations with experiments from [17].

Simulations corresponding to an abrupt p–n junction (i.e. D_W=0) yield instead an R_{n1}^{odd} much smaller than in ex-

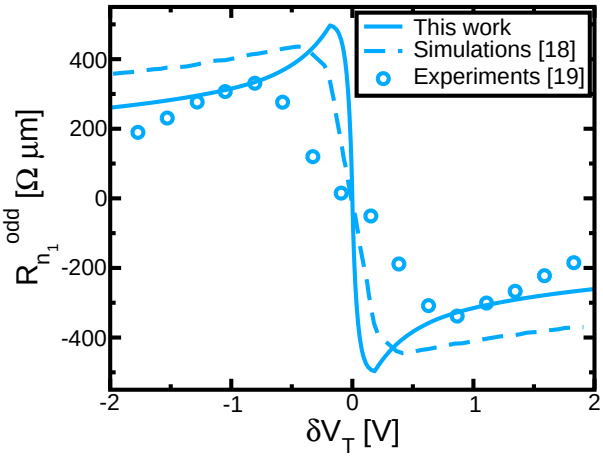


Figure 5: Odd resistance versus δV_T. The carrier density in region 1 is $n_1 \simeq 0.51 \cdot 10^{12}$ cm^{-2} and the temperature is T=300 K. The dashed line displays the simulation results obtained in [18], symbols are experiments from [19], and the solid line shows the results of this work for a p–n junction width D_W=50 nm.

periments, while for D_W=50 nm our calculations can track experiments quite well in the entire n_1, c_2 range. Similar results for D_W=50 nm were found in [16].

As an additional validation of our model for the ballistic p–n junction, in Fig. 5 we show the *odd resistance* as a function of $\delta V_T = V_T - V_{T0}$, where V_T is the top gate voltage and V_{T0} is the voltage at which the difference between the Fermi level and the Dirac energy in the region 2 is equal to 0 in the test-structure sketched in Fig. 4a. The results of our model are compared to the simulation results from [18], as well as to the experimental data in [19]. To reproduce the R^{odd}_{n1}–δV_T curves we have considered the device structure in Fig. 4a with $n_1 \simeq 0.51 \cdot 10^{12}$ cm^{-2}, D_W=50 nm and T=300 K. To calculate the Dirac energy with respect to the Fermi level in the region 2 at each voltage V_T we used the electrostatic model in [18] which is similar to that described in Section IV-A for graphene. Our calculations are fairly close to previous simulations and experiments [18, 19].

The results in Fig. 4b and Fig. 5 suggest that a ballistic transport model can describe the resistance of graphene p–n junctions with D_W up to some tens of nanometers, consistently with the long mean free paths in graphene [14, 15].

IV. Implications for Dirac-Source FETs

In Fig. 6(a) we show a sketch of an n–type DS-FET. As we can see, we have a graphene p–n junction in the access region of this device. In this section, we will describe the current I_{DS} of a DS-FET including the influence of such p–n junction, based on the model developed in Section II. Then we will present simulation results of the I_{DS} versus V_G characteristics for a template DS-FET.

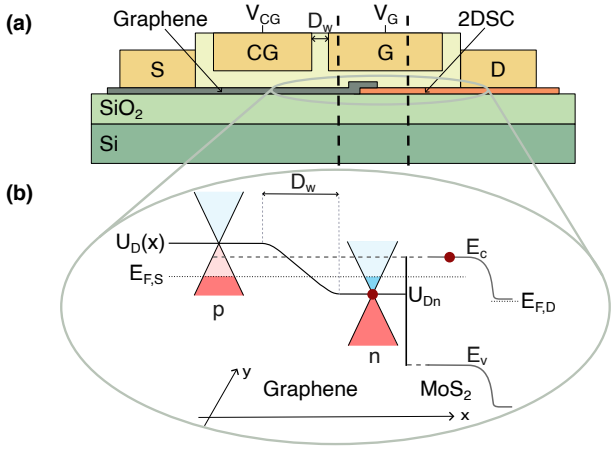


Figure 6: **(a)** Sketch for a graphene–MoS_2 n–type DS-FET, where CG and G are the control-gate and conventional gate terminal. **(b)** Band diagram in a zoomed region of the DS-FET. U_{Dn} is the Dirac energy in the n–type graphene and E_C is the MoS_2 conduction band minimum. D_W is the width of the p–n graphene junction.

A. A Basic Model for the Dirac-Source FET

We here introduce a simple model for the n–type DS-FET sketched in Fig. 6(a), whereby I_{DS} is given by the thermionic injection of electrons from the graphene source into the conduction band of the 2D semiconductor material (2D-SCT) in the transistor channel. We assume ballistic transport, implying also the conservation of the transverse momentum $\hbar k_y$ along the transport path. Therefore, for a given energy E, the condition for the thermionic injection into the 2D-SCT becomes $E > E_C + \hbar^2 k_y^{\,2}/(2m_c)$, where m_c is the conduction band effective mass of the 2D-SCT. Moreover, we also assume that the available electronic modes are limited by the graphene source, due to a much larger availability of modes in the conduction band of the 2D-SCT [9].

Hence, we can calculate the current I_{DS} by adapting Eq. (12) to an n-type DS-FET. In particular, we here consider a V_{DS} large enough that the Fermi function $f_{0,D}$ at the drain reservoir is negligible compared to the $f_{0,S}$ at source (in the E range of interest), so that we have

$$I_{DS} = \frac{2 n_v q}{h} \frac{W_y}{2\pi} \int_{E_C}^{+\infty} dE \int_{-\infty}^{+\infty} dk_y \, T(E, k_y) f_{0,S} \qquad (15)$$

where n_v is the valley degeneracy of graphene, $T(E, k_y)$ is the transmission coefficient across the graphene p–n junction calculated through Eq. (11). The conservation of $\hbar k_y$ implies that the $T(E, k_y)$ in Eq. (15) is zero for $\hbar |k_y| > \sqrt{2m_c(E - E_C)}$. Moreover, as already mentioned in the comment to Eq. (12), the integral over k_y in Eq. (15) can be restricted to $|k_y| \leq \min(k_0, k_N)$ with $k_{0(N)} = |E - U_D(x_{0(N)})|/(\hbar v_f)$.

Our model is in spirit similar to the virtual source model widely used for nanoscale MOSFETs [20]. Similarly to [9], we do not attempt a physical description of the interlayer tunneling between the graphene and the 2D-SCT layer, but we assume instead a perfect transmission equal to 1.0. A more rigorous treatment of such an interlayer tunnelling is beyond

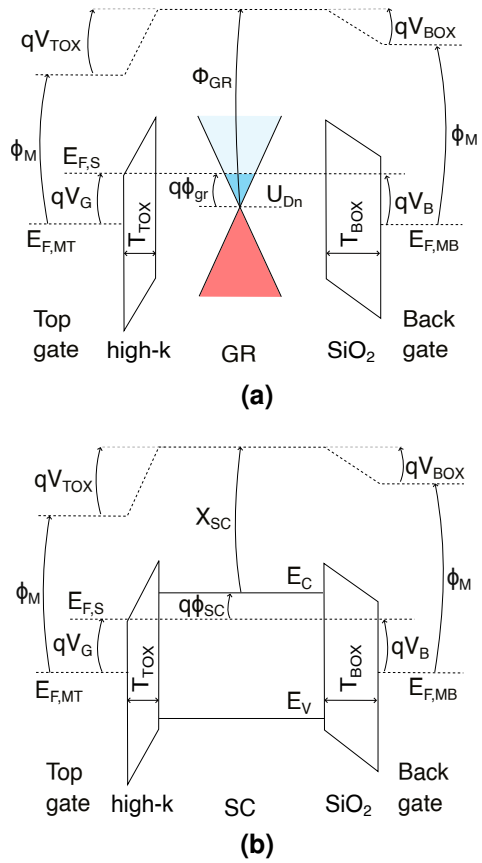


Figure 7: **(a)** Band diagram along the vertical direction for the graphene region overlapped by the gate in a DS-FET (see the leftmost, vertical dashed line in Fig. 6(a)). Φ_{GR} is the graphene workfunction, ϕ_M is the metal gate workfunction, $E_{F,MT}$ and $E_{F,MB}$ are the Fermi levels of the top and back gate, V_G and V_B are the top and back gate voltages, V_{TOX} and V_{BOX} are the top and back oxide voltages, T_{TOX} and T_{BOX} are the top and back oxide thickness, $E_{F,S}$ is the Fermi level in the source, U_{Dn} is the Dirac energy in the n-type graphene and $q\phi_{gr}$ is defined as $q\phi_{gr}$=$(E_{F,S} - U_{Dn})$. **(b)** Band diagram in the MoS_2 section of a DS-FET (see rightmost vertical, dashed line in Fig. 6(a)). $\mathcal{X}_{SC}$ is the semiconductor electron affinity, E_C and E_V are the energies of the conduction and valence bands and $q\phi_{sc}$ is defined as $q\phi_{sc}$=$(E_C - E_{F,S})$. The values of the parameters used in the simulations are reported in Table II.

the scope of this work, but it is understood that the interlayer tunnelling can sizeably reduce I_{DS}, which is indeed a design challenge for DS-FETs [21][22].

In order to obtain I_{DS} from Eq. (15), for any given gate voltage V_G we need to calculate U_{Dn} and E_C (see Fig. 6). In fact, the transmission coefficient $T(E, k_y)$ across the graphene p−n junction is set by the Dirac energies in the p-type and n-type regions. In particular, the Dirac energy in the p-type region is set by the control gate voltage V_{CG}. The Dirac energy U_{Dn} in the graphene region overlapped by the gate, instead, is modulated by the gate voltage V_G.

To link U_{Dn} and E_C to V_G, we developed a one-dimensional electrostatic model for the graphene and the 2D-SCT gated regions, similar to the model discussed in [21]. To this purpose, we first define $q\phi_{gr}$=$E_{F,S}$−U_{Dn} (see Fig. 7a), and write the electron and hole concentration as

$$n(\phi_{gr}),\, p(\phi_{gr}) = \frac{2}{\pi}\left(\frac{K_B T}{\hbar v_f}\right)^2 \mathcal{F}_1\left(\pm\frac{q\phi_{gr}}{K_B T}\right) \tag{16}$$

where $\mathcal{F}_1$ is the Fermi integral of order one, and the upper and lower sign applies to respectively electrons and holes. Equation (16) assumes that the carrier concentrations are in equilibrium with the source Fermi level $E_{F,S}$. Then, the sheet charge in graphene is linked to the electric displacement in the top and back oxide as

$$\begin{aligned} &C_{TOX}\, V_{TOX} + C_{BOX}\, V_{BOX} = \\ &= -q\,[p\,(\phi_{gr}) - n\,(\phi_{gr})] \end{aligned} \tag{17}$$

where V_{TOX} and V_{BOX} are defined in Fig. 7a and C_{TOX}=$\frac{\varepsilon_{TOX}}{T_{TOX}}$, C_{BOX}=$\frac{\varepsilon_{BOX}}{T_{BOX}}$. Based on the band-diagram in Fig. 7a, we can link V_{TOX} and V_{BOX} to V_G and V_B as

$$qV_{TOX} = \Phi_{GR} - q\phi_{gr} + qV_G - \phi_M \tag{18a}$$

$$qV_{BOX} = \Phi_{GR} - q\phi_{gr} + qV_B - \phi_M \tag{18b}$$

By inserting Eq. (18) and Eq. (16) in Eq. (17), we find an equation for the unknown $q\phi_{gr}$, which provides $q\phi_{gr}$=$E_{F,S}$−U_{Dn} as a function of V_G (assuming V_B=0).

A similar approach can be used to calculate E_C in the 2D-SCT. We first define $q\phi_{sc}$=$(E_C$−$E_{F,S})$ (see Fig. 7b). Then we write the electron concentration in the 2D-SCT as

$$n(\phi_{sc}) = \frac{1}{2}\frac{2\, m_c\, n_v}{2\pi\hbar^2} K_B T ln\left(1 + e^{-\frac{q\phi_{sc}}{K_B T}}\right) \tag{19}$$

where m_c is the effective mass and n_v the valley degeneracy in the conduction band of the 2D-SCT. Equation (19) assumes a ballistic transport regime, whereby the states having a positive velocity component $\hbar k_x/m_c$ along x are in equilibrium with $E_{F,S}$ and, moreover, the states with a negative k_x are practically empty for a V_{DS} much larger than $K_B T/q$.

For the 2D-SCT we can write equations similar to the Eqs. (17) and (18) for graphene. For the electric displacements in the oxides we have

$$C_{TOX} V_{TOX} + C_{BOX} V_{BOX} = q\, n(\phi_{sc}) \tag{20}$$

and for the link between ϕ_{sc} and external voltages we have

$$qV_{TOX} = \mathcal{X}_{SC} + q\phi_{sc} + qV_G - \phi_M \tag{21a}$$

$$qV_{BOX} = \mathcal{X}_{SC} + q\phi_{sc} + qV_B - \phi_M \tag{21b}$$

By inserting Eq. (21) and Eq. (19) in Eq. (20), we find an equation in the unknown $q\phi_{sc}$, which allows us to calculate $q\phi_{sc}$=$(E_C$−$E_{F,S})$ as a function of V_G.

B. Simulations results

Fig. 8 shows the calculated I_{DS} versus V_G characteristics for a DS-FET with a source carrier concentration p≈8.75×10^{12}cm^{-2}, and for different widths D_W of the p−n junction. In actual devices, D_W is lower limited by the alignment of the CG and G gates, hence a D_W in the range between 20 and 30 nm is already a very aggressively scaled value. The sub-60 mV/dec behavior is clearly observed in

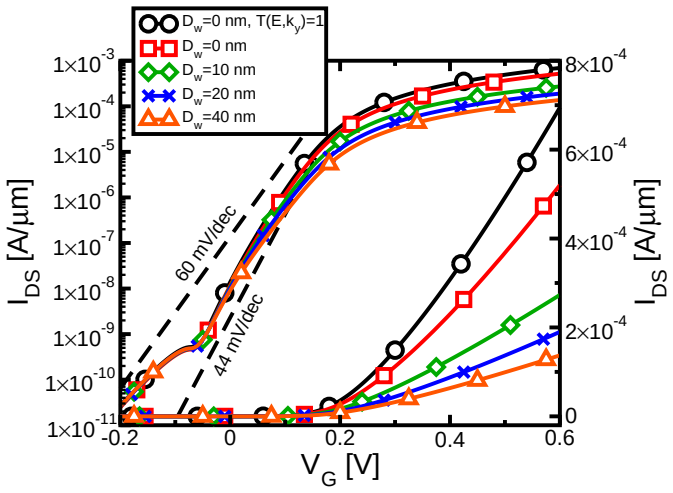


Figure 8: Simulated I_{DS} versus V_G characteristics of a DS-FET at V_{DS}=0.3 V and for different D_W values of the $p-n$ junction. Results obtained for $T(E,k_y)$=1.0 are reported for comparison. The hole concentration in the source is $p\approx 8.75\times10^{12}$cm^{-2}. The metal gate workfunction Φ_M=4.33 eV allows us to have I_{OFF}=10 nA/μm at V_G=0 V. The other material parameters can be found in Table II.

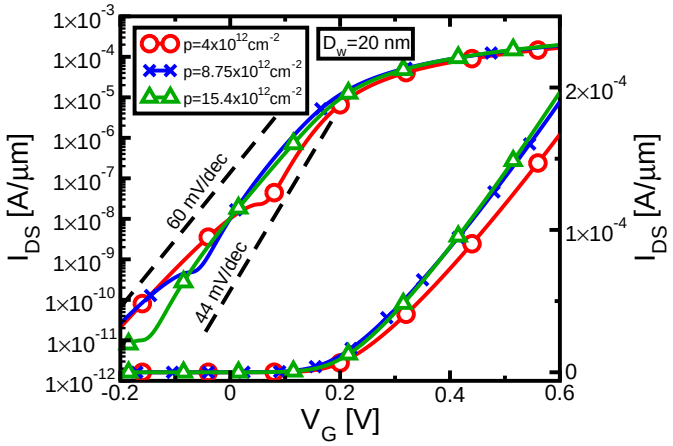


Figure 9: Same simulations as in Fig. 8 for D_W=20 nm and V_{DS}=0.3 V, but for different values of the hole concentration, p, in the source. The concentrations $p\approx 4\times10^{12}$, 8.75×10^{12} and 15.4×10^{12} cm^{-2} correspond to $(U_{Dp}-E_{F,S})$ equal to respectively 0.2 eV, 0.3 eV and 0.4 eV, where U_{Dp} is the Dirac energy in the source. The metal gate workfunction for $p\approx4\times10^{12}$cm^{-2} and $p\approx15.4\times10^{12}$cm^{-2} has been tuned so that the off-current is $I_{OFF}\approx$10 nA/μm at V_G=0 in all cases.

Parameter	Symbol	Value
Metal gate workfunction	ϕ_M	4.33 eV
Graphene workfunction	Φ_{GR}	4.5 eV
Semiconductor affinity (MoS_2)	$\mathcal{X}_{SC}$	4.1 eV
Top oxide thickness	T_{TOX}	5 nm
Back oxide thickness	T_{BOX}	20 nm
Top oxide dielectric constant	ε_{TOX}	$20\varepsilon_0$
Back oxide dielectric constant (SiO_2)	ε_{BOX}	$3.9\varepsilon_0$
Back gate voltage	V_B	0 V
Effective mass (MoS_2)	m_c	$0.51m_0$
Valley degeneracy (MoS_2, graphene)	n_v	2

Table II: Material parameters for graphene and for the 2D semiconductor, MoS_2, used throughout the work (if not otherwise stated).

the sub-threshold region. In the on-state, the resistance of the $p-n$ junction substantially degrades the device current. In particular, it can be seen that the calculations assuming $T(E,k_y)\simeq$1.0 result in I_{DS} values similar to those reported in [9], but substantially larger than the I_{DS} values obtained by accounting for the $p-n$ access region. In this respect we note that, in experimental studies dealing with graphene-MoS_2 DS-FETs, the reported on-currents are in the range of tens of μA/μm [6, 7], suggesting that either the interlayer tunneling or other extrinsic effects may limit I_{DS}. For example, the contact resistance to single-layer graphene is a notorious challenge, with the best values reported for CVD graphene and sputtered or evaporated metals ranging between some hundreds $\Omega\cdot\mu$m to a few $k\Omega\cdot\mu$m [23]. Therefore, the contact resistance to graphene could also degrade the on-state I_{DS} [10].

Fig. 9 shows the calculated I_{DS} versus V_G characteristics of a DS-FET for different hole concentrations at the source and for D_W=20 nm. The steep part of the sub-threshold region shifts to smaller I_{DS} values for increasing hole concentrations at the source. This is because, for larger hole concentrations, the Dirac energy U_{Dp} raises higher above the source Fermi level $E_{F,S}$. Hence, the electronic states around U_{Dp}, which are responsible for the steep slope behavior, are progressively de-populated by increasing the hole concentration, namely the I_{DS} in the sub-60mV/dec region becomes smaller.

V. Discussion and Conclusions

We have presented a semi-analytical model for a graphene DS-FET based on the transfer-matrix method. The model includes the finite ballistic resistance of the graphene p–n junction, which is substantially influenced by the transition width, D_W, of the junction. Our model for the p–n junction resistance was validated against both previous experiments and theoretical calculations.

Our results indicate that, in graphene DS-FETs, the resistance of the graphene p–n junction plays an important role for the on-state I_{DS} of the devices. In fact, the current is influenced by the transition width D_W of the junction, as well as by the hole concentration p in the source region.

The main goal of this paper was to develop a model for the $p{-}n$ junction in the access region of a graphene DS-FET, and then to show that the finite ballistic resistance of a $p{-}n$ junction has a sizeable impact on the on-state current of the transistor. We acknowledge, however, that our description of the DS-FET is likely to be over-optimistic, as it does not account for some relevant non-idealities.

As for the role of inelastic phonon-scattering, for example, we think that a quantitative assessment of its influence via simulations remains very difficult, particularly for DS-FETs based on van der Waals heterojunctions. In fact a realistic description of the phonon spectra and of the electron-phonon interaction is very challenging in heterojunctions. In this respect, however, we recall that sub-60mV/dec values for the subthreshold swing have been experimentally reported in graphene-MoS_2 systems at room temperature [6, 7]. Clearly, further experimental and theoretical work is necessary to enlighten the impact of electron-phonon interaction in DS-FETs.

As for the comparison between simulations and experiments, the simulations have shown that even a small graphene bandgap opening can result in a sizeable improvement of the subthreshold swing in graphene-based DS-FETs [8, 24]. We have independently observed a similar behavior with our modeling approach (not shown). Therefore, we think that a possibly unintentional bandgap opening in graphene could influence the best experimental values reported for the subthreshold swing in DS-FETs.

Moreover, a lattice misalignement between graphene and the semiconductor appears almost inevitable with most transfer techniques. The influence of a rotational misalignment has been discussed for interlayer tunneling FETs based on van der Waals heterojunctions [25], as well as for doped graphene-insulator-graphene junctions with complementary doping [26] [27]. The magnitude and peak width of the resonant tunnelling current in graphene-insulator-graphene junctions have been shown to be sensitive to the rotational misalignment of the two graphene layers [26] [27]. In the interlayer tunneling FETs, instead, the rotational misalignment between the two different 2D materials can for sure reduce the absolute value of the tunneling current, but it is not expected to affect the bias dependence and, in particular, the possible steepness of the subthreshold region [25]. Therefore, while a lattice misalignment between graphene and the semiconductor can affect the current of heterojunction DS-FETs, it does not necessarily hinder the steepness of the subthreshold operation.

Acknowledgements: This work was partially supported by the European Union through the AttoSwitch project (GA:101135571).

APPENDIX A
PROBABILITY FLUX IN GRAPHENE

To find the expression of the probability flux $J_{\bar{\varphi}}$ in Eq. (3) we can start by writing the probability continuity equation:

$$\frac{\partial \left|\overline{\varphi}(\bar{r},t)\right|^2}{\partial t} + \nabla \overline{J}_{\overline{\varphi}}(\bar{r},t) = 0. \tag{22}$$

Then, by recalling $\overline{\varphi}(\bar{r},t)=\begin{pmatrix}\varphi_1(\bar{r},t)\\ \varphi_2(\bar{r},t)\end{pmatrix}$, we have

$$\begin{aligned}\frac{\partial \left|\overline{\varphi}\right|^2}{\partial t} &= \frac{\partial \left|\varphi_1\right|^2}{\partial t} + \frac{\partial \left|\varphi_2\right|^2}{\partial t} = \\ &= \varphi_1^* \frac{\partial \varphi_1}{\partial t} + \varphi_1 \frac{\partial \varphi_1^*}{\partial t} + \varphi_2^* \frac{\partial \varphi_2}{\partial t} + \varphi_2 \frac{\partial \varphi_2^*}{\partial t}\end{aligned} \tag{23}$$

By substituting in Eq. (23) the expressions for $\frac{\partial \varphi_1}{\partial t}$ and $\frac{\partial \varphi_2}{\partial t}$ from Eq. (1) we readily find

$$\frac{\partial \left|\overline{\varphi}\right|^2}{\partial t} = v_f \left[-\frac{\partial}{\partial x}(\varphi_1^*\varphi_2{+}\varphi_1\varphi_2^*){+}i\frac{\partial}{\partial y}(\varphi_1^*\varphi_2{-}\varphi_1\varphi_2^*)\right] \tag{24}$$

By comparing Eq. (24) and Eq. (22), we can identify the components of the probability flux as

$$(J_{\bar{\varphi},x}, J_{\bar{\varphi},y}) = v_f \left[\varphi_1^*\varphi_2 + \varphi_1\varphi_2^*, -i\left(\varphi_1^*\varphi_2 - \varphi_1\varphi_2^*\right)\right]. \tag{25}$$

which can be recognized as the expressions in Eq. (3).

APPENDIX B
WAVE-FUNCTIONS AND TRANSMISSION IN A GRAPHENE p–n JUNCTION

Considering a region where $U_D(x){=}U_0$ is constant and recalling the *ansatz* $\overline{\psi}(\bar{r}){=}\begin{pmatrix}\psi_1(x)\\ \psi_2(x)\end{pmatrix}e^{ik_y y}$, we multiply Eq. (4) by $(E{-}U_0)$ and derive Eq. (4)(b) with respect to x, so as to obtain:

$$-(E-U_0)i\hbar v_f\left(\frac{\partial \psi_2}{\partial x} + k_y\psi_2\right) = (E-U_0)^2\,\psi_1 \tag{26a}$$

$$-(E-U_0)i\hbar v_f\left(\frac{\partial^2 \psi_1}{\partial x^2} - k_y\frac{\partial \psi_1}{\partial x}\right) = (E-U_0)^2\,\frac{\partial \psi_2}{\partial x} \tag{26b}$$

Assuming $E{\neq}U_0$, we substitute Eq. (4)(b) and Eq. (26)(b) in Eq. (26)(a) and find

$$\frac{\partial^2 \psi_1}{\partial x^2} = -\frac{1}{\hbar^2 v_f^2}\left[(E-U_0)^2 - \hbar^2 v_f^2 k_y^2\right]\psi_1. \tag{27}$$

For $E{>}[U_0{+}\hbar v_f|k_y|]$ or $E{<}[U_0{-}\hbar v_f|k_y|]$ the factor multiplying ψ_1 in the r.h.s. of Eq. (27) is negative. Hence, by using the k_x defined in Eq. (5), Eq. (27) can be solved as:

$$\psi_1(x) = Ae^{ik_x x} + Be^{-ik_x x} = \psi_{1PP}(x) + \psi_{1RP}(x) \tag{28}$$

where $\psi_{1PP}(x){=}Ae^{ik_x x}$ is a progressive propagating wave and $\psi_{1RP}(x){=}Be^{-ik_x x}$ is a regressive propagating wave. Substituting $\psi_{1PP}(x)$ in Eq. (4)(b) we find

$$\psi_{2PP}(x) = s_{cv}\,\psi_{1PP}(x) \times \frac{k_x + ik_y}{k} \tag{29}$$

where $s_{cv}{=}1$ if $E{>}U_0$ and $s_{cv}{=}{-}1$ if $E{<}U_0$. Analogously, substituting $\psi_{1RP}(x)$ in Eq. (4)(b) we find

$$\psi_{2RP}(x) = s_{cv}\,\psi_{1RP}(x) \times \frac{-k_x + ik_y}{k}. \tag{30}$$

Hence, by introducing $\theta_{\bar{k}}{=}\text{arctg}\,(k_y/k_x)$ for $k_x{>}0$, we can rewrite $\psi_{2PP}(x)$ and $\psi_{2RP}(x)$ as

$$\psi_{2PP}(x) = s_{cv}\,\psi_{1PP}(x)\,e^{i\theta_{\bar{k}}} = s_{cv}\,A\,e^{i(k_x x + \theta_{\bar{k}})} \tag{31}$$

$$\psi_{2RP}(x) = s_{cv}\,\psi_{1RP}(x)(-e^{-i\theta_{\bar{k}}}) = -s_{cv}\,B\,e^{-i(k_x x+\theta_{\bar{k}})} \quad (32)$$

By writing $\psi_1(x)$ and $\psi_2(x)$ as the sum of a progressive and a regressive propagating wave, we finally obtain Eqs. 6(a),(b).

A similar derivation can be developed for the case $U_0-\hbar v_f|k_y|<E<U_0+\hbar v_f|k_y|$. Now we use the γ_x defined in Eq. (7) and see that Eq. (27) can be readily solved as:

$$\psi_1(x) = Ae^{\gamma_x x} + Be^{-\gamma_x x} = \psi_{1PE}(x) + \psi_{1RE}(x) \quad (33)$$

where $\psi_{1PE}(x)=Ae^{\gamma_x x}$ is a wave-function evanescent in the positive x direction, whereas $\psi_{1RE}(x)=Be^{-\gamma_x x}$ is evanescent in the negative x direction. By substituting $\psi_{1PE}(x)$ in Eq. (4)(b) we find

$$\psi_{2PE}(x) = i\,s_{cv}\,\psi_{1PE}(x)\frac{k_y-\gamma_x}{\sqrt{k_y^2-\gamma_x^2}}. \quad (34)$$

We now note that for $k_y<0$ we have $(k_y-\gamma_x)<0$, and for $k_y>0$ we also have $(k_y-\gamma_x)>0$ (because γ_x is smaller than $|k_y|$, see Eq. (7)), therefore we can write $(k_y-\gamma_x)=\text{sign}(k_y)|k_y-\gamma_x|$. We now recall the definition of ξ in Eq. (7) and see that Eq. (34) can be rewritten as

$$\psi_{2PE}(x) = i\,s_{cv}\,\xi\,\psi_{1PE}(x). \quad (35)$$

Analogously, by substituting $\psi_{1RE}(x)$ in Eq. (4)(b) we find

$$\psi_{2RE}(x) = i\,s_{cv}\,\psi_{1RE}(x)\,\frac{k_y+\gamma_x}{\sqrt{k_y^2-\gamma_x^2}}. \quad (36)$$

finally leading to

$$\psi_{2RE}(x) = i\,s_{cv}\,\xi^{-1}\,\psi_{1RE}(x). \quad (37)$$

If we now write $\psi_1(x)$ and $\psi_2(x)$ as the sum of the two evanescent waves, we finally obtain Eqs. 8(a),(b).

The expressions for the propagating wave-functions in Eq. (6) can be used in Eq. (3) to calculate the corresponding probability flux. By doing so, the x component $J_{\overline{\varphi},x}(E)$ of the flux at the energy E can be written as

$$J_{\overline{\varphi},x}(E) = 2v_f s_{cv}\frac{k_x}{k}\left(|A|^2-|B|^2\right) \quad (38)$$

where $s_{cv}=-1$ if $E<U_0$ and $s_{cv}=1$ if $E>U_0$. As it can be seen, if we consider an energy E in the valence band (i.e. for $E<[U_0-\hbar v_f|k_y|]$), the positive flux is carried by $Be^{-ik_x x}$ and the negative flux is carried by $Ae^{ik_x x}$. If we consider an energy E in the conduction band (i.e. for $E>[U_0+\hbar v_f|k_y|]$), instead, $Ae^{ik_x x}$ gives the positive flux and $Be^{-ik_x x}$ gives the negative flux.

The expression of the flux in Eq. (38) has been exploited to compile Table I, namely to identify the entries of the matrix $[MT]$ that govern the transmission $T(E,k_y)$ in a graphene p–n junction. If we consider, for example, the energy E in the band diagram of Fig. 2a, we see that E belongs to the valence band in the p-type region and to the conduction band in the n-type region. Therefore, the positive flux at the energy E is given by $J^{(p)}_{\overline{\varphi},x}=2v_f(k_{x,0}/k_0)|B_0|^2$ in the p-type, and by $J^{(n)}_{\overline{\varphi},x}=2v_f(k_{x,N}/k_N)|A_N|^2$ in the n-type region. The transmission coefficient is thus given by

$$T(E,k_y) = \frac{J^{(n)}_{\overline{\varphi},x}}{J^{(p)}_{\overline{\varphi},x}} = \frac{k_{x,N}}{k_N}\frac{k_0}{k_{x,0}}\frac{|A_N|^2}{|B_0|^2} \quad (39)$$

where k_0, $k_{x,0}$ and k_N, $k_{x,N}$ are the magnitude and the x component of the wave-vector respectively in the left-most element and in the right-most element. By setting $B_N=0$, we have $B_0=MT_{2,1}A_N$ and we finally obtain

$$T(E,k_y) = \frac{k_{x,N}}{k_N}\frac{k_0}{k_{x,0}}\frac{1}{|MT_{2,1}(E,k_y)|^2} \quad (40)$$

A similar approach can be used for the other three cases summarized in Table I.

REFERENCES

[1] S. Datta, W. Chakraborty, and M. Radosavljevic. "Toward attojoule switching energy in logic transistors". In: *Science* 378.6621 (Nov. 2022), pp. 733–740. DOI: 10.1126/science.ade7656.

[2] A. C. Seabaugh and Q. Zhang. "Low-Voltage Tunnel Transistors for Beyond CMOS Logic". In: *Proceedings of the IEEE* 98.12 (Dec. 2010), pp. 2095–2110. DOI: 10.1109/JPROC.2010.2070470.

[3] D. Esseni, M. Pala, P. Palestri, C. Alper, and T. Rollo. "A review of selected topics in physics based modeling for tunnel field-effect transistors". In: *Semiconductor Science and Technology* 32.8 (July 2017), pp. 83005–83031. DOI: 10.1088/1361-6641/aa6fca.

[4] A. H. Castro Neto, F. Guinea, N. M. R. Peres, K. S. Novoselov, and A. K. Geim. "The electronic properties of graphene". In: *Reviews of Modern Physics* 81.1 (Jan. 2009), pp. 109–162. DOI: 10.1103/RevModPhys.81.109.

[5] C. Qiu, F. Liu, L. Xu, B. Deng, M. Xiao, J. Si, L. Lin, Z. Zhang, J. Wang, H. Guo, H. Peng, and L. Peng. "Dirac-source field-effect transistors as energy-efficient, high-performance electronic switches". In: *Science* 361.6400 (July 2018), pp. 387–392. DOI: 10.1126/science.aap9195.

[6] M. Liu, H. N. Jaiswal, S. Shahi, S. Wei, Y. Fu, C. Chang, A. Chakravarty, F. Yao, and H. Li. "Monolayer MoS2 Steep-slope Transistors with Record-high Sub-60-mV/decade Current Density Using Dirac-source Electron Injection". In: *2020 IEEE International Electron Devices Meeting (IEDM)*. 2020, pp. 12.5.1–12.5.4. DOI: 10.1109/IEDM13553.2020.9371961.

[7] Z. Tang, C. Liu, X. Huang, S. Zeng, L. Liu, J. Li, Y. Jiang, D. W. Zhang, and P. Zhou. "A Steep-Slope MoS2/Graphene Dirac-Source Field-Effect Transistor with a Large Drive Current". In: *Nano Letters* 21.4 (Feb. 2021), pp. 1758–1764. DOI: 10.1021/acs.nanolett.0c04657.

[8] F. Liu, C. Qiu, Z. Zhang, L. M. Peng, J. Wang, and H. Guo. "Dirac Electrons at the Source: Breaking the 60-mV/Decade Switching Limit". In: *IEEE Transactions on Electron Devices* 65.7 (July 2018), pp. 2736–2743. DOI: 10.1109/TED.2018.2836387.

[9] P. Wu and J. Appenzeller. "Design Considerations for 2-D Dirac-Source FETs—Part I: Basic Operation and Device Parameters". In: *IEEE Transactions on Electron Devices* 69.8 (Aug. 2022), pp. 4674–4680. DOI: 10.1109/TED.2022.3181544.

[10] E. Baccichetti and D. Esseni. "Access region resistance in graphene Dirac-Source FETs: a Transfer-Matrix based study". In: *2024 IEEE European Solid-State Electronics Research Conference (ESSERC)*. Sept. 2024, pp. 400–403. DOI: 10.1109/ESSERC62670.2024.10719492.

[11] G. J. Ferreira, M. N. Leuenberger, D. Loss, and J. C. Egues. "Low-bias negative differential resistance in graphene nanoribbon superlattices". In: *Physical Review B* 84.12 (Sept. 2011), pp. 125453–125457. DOI: 10.1103/PhysRevB.84.125453.

[12] M. I. Katsnelson, K. S. Novoselov, and A. K. Geim. "Chiral tunnelling and the Klein paradox in graphene". In: *Nature Physics* 2.9 (Sept. 2006), pp. 620–625. DOI: 10.1038/nphys384.

[13] S. Datta. *Quantum Transport: Atom to Transistor*. Cambridge University Press, June 2005. DOI: 10.1017/CBO9781139164313.

[14] F. Giannazzo, S. Sonde, R. L. Nigro, E. Rimini, and V. Raineri. "Mapping the Density of Scattering Centers Limiting the Electron Mean Free Path in Graphene". In: *Nano Letters* 11.11 (Nov. 2011), pp. 4612–4618. DOI: 10.1021/nl2020922.

[15] L. Banszerus, M. Schmitz, S. Engels, M. Goldsche, K. Watanabe, T. Taniguchi, B. Beschoten, and C. Stampfer. "Ballistic Transport Exceeding 28 μm in CVD Grown Graphene". In: *Nano Letters* 16.2 (Feb. 2016), pp. 1387–1391. DOI: 10.1021/acs.nanolett.5b04840.

[16] T. Low, S. Hong, J. Appenzeller, S. Datta, and M. S. Lundstrom. "Conductance Asymmetry of Graphene p-n Junction". In: *IEEE Transactions on Electron Devices* 56.6 (June 2009), pp. 1292–1299. DOI: 10.1109/TED.2009.2017646.

[17] B. Huard, J. A. Sulpizio, N. Stander, K. Todd, B. Yang, and D. Goldhaber-Gordon. "Transport Measurements Across a Tunable Potential Barrier in Graphene". In: *Physical Review Letters* 98.23 (June 2007), pp. 236803–236806. DOI: 10.1103/PhysRevLett.98.236803.

[18] D. Berdebes, T. Low, Y. Sui, J. Appenzeller, and M. S. Lundstrom. "Substrate Gating of Contact Resistance in Graphene Transistors". In: *IEEE Transactions on Electron Devices* 58.11 (Nov. 2011), pp. 3925–3932. DOI: 10.1109/TED.2011.2163800.

[19] Z. Chen and J. Appenzeller. "Gate modulation of graphene contacts on the scaling of graphene FETs". In: *2009 Symposium on VLSI Technology Digest of Technical Papers*. July 2009, pp. 128–129.

[20] D. Esseni, P. Palestri, and L. Selmi. *Nanoscale MOS transistors: Semiclassical modeling and applications*. Cambridge University Press, Aug. 2011. DOI: 10.1017/CBO9780511973857.

[21] M. O. Li, D. Esseni, D. Jena J. J. Nahas, and H. G. Xing. "Two-Dimensional Heterojunction Interlayer Tunneling Field Effect Transistors (Thin-TFETs)". In: *IEEE Journal of the Electron Devices Society* 3.3 (May 2015), pp. 200–207. DOI: 10.1109/JEDS.2015.2390643.

[22] D. Nguyen, A. Pilotto, D. Lizzit, M. Pala, and D. Esseni. "Sub-60mV/dec Swing and Drive Current in Dirac-Source FETs: a Design Study based on First-Principle Transport Simulations". In: *2024 IEEE International Electron Devices Meeting (IEDM)*. Dec. 2024.

[23] F. Giubileo and A. Di Bartolomeo. "The role of contact resistance in graphene field-effect devices". In: *Progress in Surface Science* 92.3 (2017), pp. 143–175. DOI: 10.1016/j.progsurf.2017.05.002.

[24] P. Wu and J. Appenzeller. "Design Considerations for 2-D Dirac-Source FETs—Part II: Nonidealities and Benchmarking". In: *IEEE Transactions on Electron Devices* 69.8 (Aug. 2022), pp. 4681–4685. DOI: 10.1109/TED.2022.3181537.

[25] M. Li, D. Esseni, G. Snider, D. Jena, and H. G. Xing. "Single particle transport in two-dimensional heterojunction interlayer tunneling field effect transistor". In: *Journal of Applied Physics* 115.7 (Feb. 2014). DOI: 10.1063/1.4866076.

[26] R.M. Feenstra, D. Jena, and G. Gu. "Single-particle tunneling in doped graphene-insulator-graphene junctions". In: *Journal of Applied Physics* 111.4 (Feb. 2012). DOI: 10.1063/1.3686639.

[27] L. Britnell, R. V. Gorbachev, A. K. Geim, L. A. Ponomarenko, A. Mishchenko, M. T. Greenaway, T. M. Fromhold, K.S. Novoselov, and L. Eaves. "Resonant tunnelling and negative differential conductance in graphene transistors". In: *Nature Communications* 4.1 (Apr. 2013). DOI: 10.1038/ncomms2817.